ACCSCIENCE PUBLISHING

International Journal of Bioprinting

RESEARCH ARTICLE

Modeling, mechanistic analysis, and control strategy for hydrogel extrusion hysteresis in piston-extrusion 3D printing

Haoran Ren[1], Zhen Wang[1,2]*, Chuanzhen Huang[1,2], Longhua Xu[1], Shuiquan Huang[1], Meina Qu[1], Zhengkai Xu[1], Dijia Zhang[1], Baosu Guo[1], Tianye Jin[1], Xiaodan Wang[1], and Bowen Li[1]

[1]School of Mechanical Engineering, Yanshan University, Qinhuangdao, Hebei, China

[2]State Key Laboratory of Crane Technology, Yanshan University, Qinhuangdao, Hebei, China

Abstract

Piston extrusion-based 3D bioprinting is a widely used technology in tissue engineering; however, the phenomenon of extrusion hysteresis severely constrains its printing accuracy. This study investigates the hysteresis mechanism using a low-viscosity gelatin hydrogel as a model material and develops effective control strategies through mathematical modeling. Rheological characterization determined the material's gelation point (29.8 °C)and the optimal printing temperature window. Subsequently, precise syringe temperature control was achieved using a heat transfer model, which exhibited a low prediction error of only 0.0065 °C. We constructed an extrusion hysteresis model that simultaneously accounts for the elastic deformation of the syringe and the compressibility of the material. A static model derived from mechanical analysis provided a formula for calculating the extrusion hysteresis volume, while a dynamic model revealed that the resulting flow rate follows an exponential decay law. Experimental validation assessed the influences of critical parameters, including piston velocity (0.020–0.030 mm/s), nozzle diameter (0.46–0.75 mm), temperature (30–35 °C), and various material types. The results demonstrated that the compressible model predictions aligned well with experimental data. However, the finest nozzle (0.46 mm) exhibited larger errors, attributed to rapid heat dissipation and increased susceptibility to premature gelation. Based on the dynamic model, we propose a control strategy employing a premature extrusion stop with adjusted movement speed. Printing experiments confirmed that for low-viscosity hydrogels, this strategy reduced accidental deposition in non-printing areas compared to standard retraction (withdrawal) strategies. This research provides a theoretical framework for optimizing the accuracy of piston extrusion systems and advances the mitigation of defects caused by extrusion hysteresis in the 3D printing of low-viscosity hydrogels.

Keywords: Piston extrusion-based 3D bioprinting; Extrusion hysteresis modeling; Dynamic control strategy; Gelatin hydrogel

***Corresponding author:**
Zhen Wang
(wangzhen@ysu.edu.cn)

Citation: Ren H, Wang Z, Huang C, *et al*. Modeling, mechanistic analysis, and control strategy for hydrogel extrusion hysteresis in piston-extrusion 3D printing. *Int J Bioprint*. 2026;12(3):026130118. doi: 10.36922/IJB026130118

Received: March 26, 2026

1st revised: April 30, 2026

2nd revised: May 11, 2026

Accepted: May 14, 2026

Published online: May 14, 2026

1. Introduction

Three-dimensional (3D) bioprinting has emerged as a pivotal manufacturing technology in tissue engineering and regenerative medicine. It enables the precise spatial deposition of biomaterials and living cells to fabricate tissue and organ models with biomimetic structures and functions, including vascularized networks,[1] artificial skin grafts,[2] and osteochondral interfaces.[3] Among various bioprinting modalities, extrusion-based bioprinting is widely utilized due to its broad compatibility with bioink viscosities, high cell-loading capacity, and the superior mechanical integrity of the printed constructs.[4,5]

Typical extrusion-based printing systems are mainly categorized into pneumatic, piston, and screw extrusion types according to the driving mode.[6] Pneumatic extrusion is the most widely used technique in gelatin-based hydrogel bioprinting. In conventional printing scenarios, negative-pressure retraction can effectively mitigate extrusion hysteresis in low-viscosity materials near the gelation point. However, for low-viscosity gelatin hydrogel in the sol state (the research object of this work), pneumatic systems have inherent limitations: the flow rate is highly sensitive to air pressure fluctuations, and even slight pressure changes cause substantial instability in extrusion volume due to the high fluidity of the material; in addition, retraction control for hysteresis mitigation is extremely difficult to regulate precisely in low-viscosity sol materials and can easily lead to over-suction, uneven material breakage, and air entrainment, thereby disrupting subsequent printing continuity. In contrast, screw extrusion systems tend to induce high shear stress, which may compromise the viability of cells in sensitive cell-laden bioinks.

Piston extrusion systems have attracted extensive attention in high-precision bioprinting of complex structures, owing to their unique advantages: direct volumetric flow control independent of material viscosity, fast dynamic response, simple structure, low cost, and convenient operation and maintenance.[7-11] Especially for low-viscosity sol hydrogels, the piston-driven mode can achieve more stable and repeatable extrusion than pneumatic systems, which is the primary rationale for selecting this driving mode in our work. Nevertheless, the inherent extrusion hysteresis effect of piston extrusion systems severely limits the flow-control advantages of piston extrusion systems, and has become a key bottleneck limiting the printing accuracy of low-viscosity hydrogels. Recently, the integration of real-time monitoring within piston-driven systems has further enhanced their reliability in handling complex hydrogels,[12] but the mechanism analysis and quantitative control of extrusion hysteresis still lack systematic research.

In the optimization research of piston extrusion systems, the attention of the academic and engineering communities is usually focused on nozzle path planning, the regulation of material rheological properties, and biological characterization,[13] as well as the development of advanced process control strategies.[14] Gómez-Blanco *et al.*[15] systematically compared the extrusion flow field characteristics of pneumatic and piston-driven bioprinting using computational fluid dynamics simulations and experimental validation, and clarified that piston-driven mode can achieve more stable volumetric flow control with lower dispensing pressure, which further verified the unique advantages of piston extrusion systems in high-precision bioprinting. These strategies increasingly incorporate integrated pneumatic and thermal controls,[16] along with closed-loop quality control systems to ensure extrusion accuracy.[17]

Extrusion hysteresis refers to the phenomenon where, to ensure the sealing between the piston and the syringe and guarantee smooth piston movement, the system typically employs elastic seals. During extrusion, the pressure exerted by the piston causes elastic deformation of the syringe; when the piston stops moving, the elastic potential energy stored in the deformed syringe is continuously released, generating sustained pressure on the bioink and leading to unintended extrusion of material after the stop command. However, the "extrusion hysteresis" phenomenon in the printing process has long been overlooked, and it gives rise to two major issues: first, at the endpoint of the printing path, abnormal material accumulation occurs, disrupting the geometric uniformity and dimensional accuracy of the structure; second, during the non-printing movement of the print head, extrusion hysteresis can cause material contamination of non-target areas, affecting interlayer adhesion and print quality. Such structural inaccuracies directly compromise the mechanical integrity of the printed scaffold and disrupt the uniform spatial distribution of the encapsulated cells.[18,19] Unlike the pressure relaxation in pneumatic systems or inertial overshoot in screw systems, the root cause of piston-extrusion hysteresis lies in the accumulation and release of elastic deformation energy under solid–fluid coupling, which is difficult to eliminate through simple motion command delays or retraction strategies.

Although extrusion hysteresis has a significant impact on printing quality, there is currently a lack of targeted modeling and mechanism studies on the hysteresis phenomenon in piston extrusion systems. Therefore, the accurate modeling and quantitative analysis of extrusion hysteresis behavior is an urgent requirement for improving the accuracy and reliability of piston extrusion-based bioprinting.

To enable research on the extrusion hysteresis phenomenon, this study selected gelatin hydrogel in the sol state as the experimental material. First, the rheological behavior of the material in the sol state is simpler and more stable, which facilitates the construction of an accurate physical model without the complex rheological interactions typically observed in formulated bioinks.[20,21] Understanding these fundamental rheological parameters is essential for analyzing extrusion behaviors.[22] When the temperature is above the gelation point, the material exhibits a sol state; selecting the gel in the sol state for printing can eliminate the complex interference caused by the phase transition of the material. Highly dynamic rheological changes during the sol–gel transition are known to cause inconsistent flow rates and severe nozzle clogging, drastically reducing print reproducibility.[23,24] To enable the material in the sol state to retain its shape during printing, Zhou *et al.*[25] achieved rapid gelation of the material at body temperature by using microbial transglutaminase and gelatin, which not only results in simple and stable rheological behavior during flow with minimal cell damage but also enables the fabrication of printable models. If the material is in the gel state or undergoes a sol–gel transition during printing, it will exhibit strong viscoelasticity, thixotropy, and even yield stress,[26] leading to discontinuous and non-uniform extruded filaments that ultimately compromise the printability and structural shape fidelity of the constructs.[27] Meanwhile, high shear stress can compromise cell viability. Under gel-state or sol–gel transition conditions, multiple factors can affect the extrusion hysteresis volume, and precise temperature control is required to maintain consistent rheological properties during the experiment, with the resulting extrusion hysteresis volume being significantly influenced by extrusion time. Stabilizing the material in the sol state through temperature control can reduce the impact of inconsistent deformation and forces during extrusion on the results.[28-30]

In non-industrial-grade bioprinters, the heating system often struggles to achieve precise temperature control due to factors such as the air thermal resistance between the syringe and the heating sleeve, as well as heat exchange with the external environment. Even when thermal equilibrium is reached, there is typically a significant deviation between the actual temperature of the syringe and the setpoint. Hydrogels are primarily composed of water, which has a large specific heat capacity and results in a slow heating process. Therefore, precise control of the temperature field is a prerequisite for ensuring the repeatability of the printing process and a necessary foundation for independently studying the mechanical extrusion hysteresis phenomenon.[31]

Simulation methods and computational modeling are commonly used to study the temperature field distribution and optimize thermal control in 3D printing. For example, Gao *et al.*[31] altered the characteristic length of the heating structure, qualitatively analyzed the influence of characteristic length on heating uniformity using a physical model, and subsequently used finite element simulation to regulate the spatial uniformity of the temperature field.

This work makes three contributions: it establishes a comprehensive predictive model for piston-extrusion hysteresis that integrates syringe elasticity, material compressibility, and temperature control; experimentally reveals the exponential decay of hysteresis flow rate over time; and proposes a dynamic feedforward control strategy that outperforms conventional constant-speed methods.

2. Materials and methods

2.1. Preparation of gelatin material

In this experiment, Type A gelatin (bloom strength approximately 300 g; Sigma-Aldrich, United States of America), sodium alginate (Aladdin, China), and glycerol (Sinopharm Chemical Reagent, China) were used as the raw materials.

For the preparation of the pure gelatin hydrogel solution, gelatin powder was dissolved in deionized water to obtain a 10% mass-fraction gelatin hydrogel solution. The mixture was stirred magnetically at 50 °C and 500 rpm for at least 30 min to ensure homogeneity and remove bubbles.

For the composite gelatin solution, 8 g gelatin, 1 g sodium alginate, and 5 g glycerol were dissolved in 86 g deionized water to prepare 100 g of solution containing 8 wt% gelatin, 1 wt% sodium alginate, and 5 wt% glycerol. To prevent sodium alginate powder from aggregating, the powder was added gradually in several portions under continuous stirring until completely dissolved. The mixed solution was then placed in a 37 °C water bath and subjected to ultrasonic defoaming until no visible bubbles remained.

To facilitate observation during subsequent printing, blue food coloring was added to both solutions at a mass fraction of 0.1%.

A rotational rheometer (HAAKE MARS 40, Thermo Scientific HAAKE, Germany) was used to perform rheological tests on the hydrogel to determine the gelation point and evaluate its temperature dependence. First, a temperature sweep test was conducted: the oscillation frequency was set to 1 Hz, the strain was controlled at 1%, and the sample was incubated at 25 °C for 10 min to eliminate thermal history. Subsequently, the temperature

was scanned from 25 °C to 31 °C at a heating rate of 1 °C/min. The gelation point of the material ($G' = G''$) was determined by monitoring the variation curves of the storage modulus (G') and the loss modulus (G'') with temperature.

To investigate the effect of temperature on the viscosity of the material at high shear rates, the shear rate was set to 100 s^{-1}, and the temperature was increased from 25 °C to 31 °C at a heating rate of 0.5 °C/min. This allowed the analysis of the influence of temperature on viscosity under high shear rate conditions.

2.2. Construction of the printing system

2.2.1. Bioprinting platform

A self-constructed three-axis bioprinter was adopted in the experiments, with its working principle illustrated in Figure 1a. The extrusion system served as the core component, where a 42-series stepper motor (0.0025 mm/step) drove the piston to propel the 5 mL plastic syringe (inner diameter D = 12.3 mm) loaded with gelatin hydrogel. The nozzle was fabricated from stainless steel, and its length (L_2) and radius (R) were set as key variables and adjusted throughout the experiments. The motion control system of the bioprinter was based on open-source firmware, and the control of extrusion and movement was realized by editing G-code.

2.2.2. Temperature control and calibration

This system used a Teflon-insulated heating wire wrapped around a stainless-steel sleeve to heat the syringe. To overcome the problem of inaccurate temperature control caused by air thermal resistance and environmental heat exchange, the study calibrated the actual temperature field inside the syringe by combining simulation with physical equations.

Based on a heat transfer model, a steady-state heat transfer equation was established, and a finite element simulation was performed using COMSOL Multiphysics software (Version 5.6, COMSOL AB, Sweden). The steady-state temperature was fitted using Minitab software (Version 19, Minitab LLC, United States of America) according to the format of the heat transfer equation, and the steady-state temperature distribution (T_3) inside the syringe under different ambient temperatures (T_0) and heating set temperatures (T_{hot}) was analyzed.

2.3. Experimental design and observation method for extrusion hysteresis

2.3.1. Experimental variable design

To systematically investigate the influencing factors of extrusion hysteresis volume (V_{hyst}), single-variable experiments were designed in this study. The experiments primarily examined the effects of piston velocity, nozzle inner diameter, material temperature, and material type on the extrusion hysteresis volume. The specific parameters are presented in Table 1.

Table 1. Experimental variables and levels

Experimental variable	Levels
Piston velocity (mm/s)	0.020, 0.025, 0.030
Nozzle inner diameter (mm)	0.46, 0.60, 0.75
Temperature (°C)	35, 32, 30
Material type	Pure gel material, composite gel material

2.3.2. Measurement of extrusion hysteresis volume

The extrusion hysteresis volume was quantified by measuring the volume of the hanging droplet at the nozzle after the piston stopped moving. To minimize errors, each parameter combination was tested four to five times with repeated measurements. The specific experimental and analytical methods are as follows: first, the piston was controlled to extrude a fixed amount of material at a preset velocity and then stopped immediately, ensuring no material was hanging at the nozzle end at the initial moment; subsequently, a high-speed camera (2,000 fps; V4.0, Hunan Rocketech Optoelectronic Technology, China) was used to record the droplet formation process, and a digital camera was employed to capture a static side view of the droplet; finally, the static image was imported into ImageJ software (Version 1.51j8, National Institutes of Health, United States of America), the droplet contour was fitted as a solid of revolution (spheroid), and the volume was calculated based on its semi-major axis a and semi-minor axis b.

2.3.3. Error control measures

To control experimental errors, the experimental process was optimized from the following two aspects: first, during each experiment, the material volume in the barrel remained constant, and the same volume is extruded in each trial, before each experiment, the syringe was heated to the set temperature and maintained at this temperature for at least 20 min before proceeding with subsequent experiments; second, the piston stop time and the start recording time

of the high-speed camera were synchronized to correct the dynamic model of hysteresis volume over time, eliminating the impact of time asynchrony during model validation.

3. Theory and calculation

3.1. Analysis of steady-state temperature distribution in the syringe

Given the difficulty in directly measuring the temperature of the material inside the syringe, this study established a predictive model for the steady-state temperature distribution within the syringe by combining heat transfer analysis with simulation methods.

The physical structure of the heating system is shown in Figure 1b, and its steady-state heat transfer process can be simplified into two series-connected parts: the first part is the heat transfer from the heating wire to the outer wall of the syringe, and the second part is the heat transfer from the outer wall of the syringe to the internal hydrogel. Based on the law of energy conservation and classical heat transfer theory,[32] the following thermal equilibrium equations can be established:

For the first part of heat transfer, the total input heat flux is denoted as $\Phi_{\text{all in}}$, while the heat convection and heat conduction in air are represented by Φ_{out} and Φ_{out2}, respectively.

The heat balance equation for the first part is:

$$\Phi_{\text{all in}}=\Phi_{\text{out}}+\Phi_{\text{out2}} \tag{1}$$

where:

$$\Phi_{all\ in}=\frac{2\pi L\lambda_1(T_{hot}-T_1)}{\ln(R_1/R_2)} \tag{2}$$

$$\Phi_{\text{out}}=h_1A_1[(T_{hot}+T_1)/2-T_0] \tag{3}$$

$$\Phi_{\text{out2}}=\frac{2\pi L\lambda_2(T_1-T_2)}{\ln(R_2/R_3)} \tag{4}$$

In the above equations, L represents the length of the syringe; T_{hot} is the temperature of the heating wire; T_1 is the

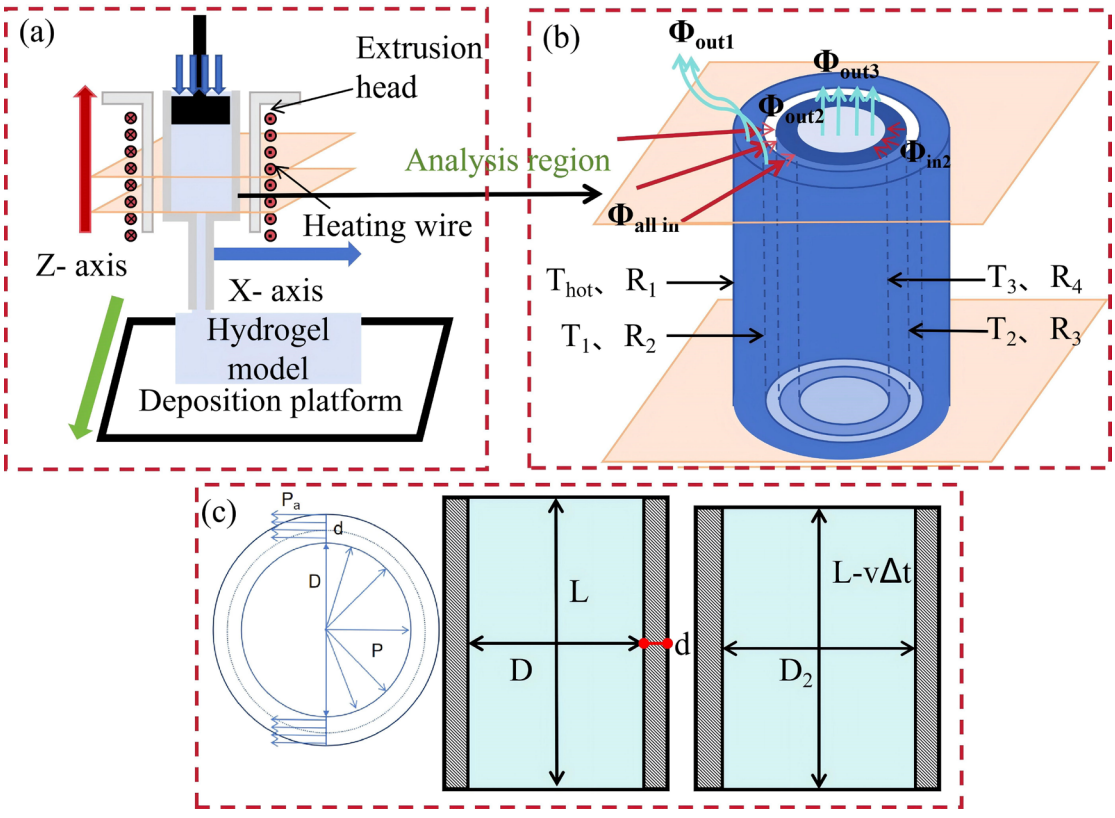

Figure 1. Schematic of piston-extrusion 3D printing structure, heat transfer, and force mechanics. (a) Piston-extrusion 3D printing principle. (b) Steady-state heat transfer in the barrel. (c) Barrel force and deformation during extrusion.

inner surface temperature of the stainless steel outer shell; T_0 is the ambient temperature; T_2 is the temperature of air at the surface of the plastic syringe; h_1 is the convective heat transfer coefficient, which could not be calculated using conventional formulas because it was closely related to the complex structure of the heating section used in this study; λ_1 is the thermal conductivity of stainless steel, which is 16 W/(m·K); λ_2 is the thermal conductivity of air, which is 0.2 W/(m·K); A_1 is the area of stainless steel exposed to air; and R_1, R_2, R_3 are the outer diameter of the stainless steel sleeve, the inner diameter of the stainless steel sleeve, and the outer diameter of the syringe, respectively.

For the second part of heat transfer, the total input heat flux is denoted as Φ_{in2}, and the heat loss to the environment is represented by Φ_{out3}.

The heat balance equation for the second part of heat transfer is expressed as $\Phi_{in2}=\Phi_{out3}$, where:

$$\Phi_{in2} = \frac{2\pi L\lambda_3(T_2 - T_3)}{\ln(R_3 / R_4)} \tag{5}$$

$$\Phi_{out3} = \lambda_4 A_2 \frac{(T_3 - T_0)}{d} \tag{6}$$

where λ_3 is the thermal conductivity of the syringe outer shell, which is 0.16 W/(m·K), A_2 is the cross-sectional area of the syringe, d is the planar wall thickness of the syringe, and λ_4 is the thermal conductivity coefficient at the material-syringe-air interface.

By combining the heat balance equations of the two processes, the final expression for the temperature T_3 inside the syringe as a function of the ambient temperature T_0 and the heating temperature T_{hot} is obtained as follows:

$$T_3 = K_1T_0 + K_2T_{hot} \tag{7}$$

Given the irregularity of the actual structure, it is difficult to obtain analytical solutions for the heat transfer coefficients K_1 and K_2. Therefore, this study adopts a finite element simulation method to simulate the temperature field under different environments, and obtains the specific values of K_1 and K_2 through linear regression fitting, thereby enabling rapid and accurate prediction of the temperature inside the syringe. This simulation-driven approach for thermal calibration has been proven highly effective in mitigating external heat loss during the extrusion bioprinting process.

3.2. Static model of extrusion hysteresis: From incompressible to compressible fluids

3.2.1. Basic assumptions and mechanical analysis

To establish a predictive model for extrusion hysteresis, the following basic assumptions are made: (i) The shear rate inside the nozzle is sufficiently high, such that the material remains in a sol state during extrusion and exhibits shear-thinning behavior. Its viscosity can be approximated by the infinite-shear viscosity, and the flow can therefore be treated as Newtonian; (ii) The flow velocity inside the syringe is low, and the pressure is considered uniform throughout the barrel; (iii) The deformation of the syringe wall remains within the linear elastic range.

Based on assumption (iii), force analysis is conducted on the syringe wall. The pressure P exerted by the piston induces a circumferential stress and elastic circumferential deformation in the syringe wall, which can be analytically described by the basic theory of thin-walled pressure vessels. The change in circumference Δx is calculated as:[33]

$$\Delta x = \frac{Fx}{EA} = PD\frac{\pi(D+d)}{2dE} \tag{8}$$

In the equation, x denotes the initial circumference of the syringe wall; Δx represents the circumferential variation of the syringe barrel wall; P is the pressure exerted by the piston; d refers to the wall thickness of the syringe; D stands for the inner diameter of the syringe; and E is the elastic modulus of the syringe material.

Figure 1c illustrates the force and deformation schematic of the syringe during piston extrusion. When the extrusion reaches a steady state, the cross-sectional area of the syringe is defined as S_1.

$$S_1 = \frac{(\pi D_2)^2}{4\pi} = \frac{(\pi D + \Delta x)^2}{4\pi} \tag{9}$$

3.2.2. Incompressible fluid model

Once a steady state is achieved, the syringe diameter remains constant, and the corresponding volumetric flow rate is given by:

$$S_1 v = Q \tag{10}$$

where v is the piston moving velocity, and Q is the volumetric extrusion flow rate.

Given the significant difference between the syringe diameter and the nozzle diameter during extrusion, the

pressure drop induced by the syringe barrel is considered negligible. Under the condition that the pressure exerted by the piston equals the pressure difference across the nozzle inlet and outlet ($P = \Delta P$), the Poiseuille equation for non-Newtonian fluids is expressed as[34]

$$Q = \pi\left(\frac{P}{2L_2K}\right)^{1/n}\frac{n}{3n+1}R^{(3n+1)/n} \tag{11}$$

where L_2 is the nozzle length, R is the nozzle radius, K denotes the consistency coefficient, and n represents the power-law index.

Based on the previous assumption that the material behaves under infinite shear rate conditions, n is set to 1 in the equation. By combining **Equations 8–11**, the pressure exerted by the piston during steady-state extrusion is derived. The condition that the piston pressure equals the pressure drop across the nozzle during extrusion is expressed as **Equation 12**:

$$P = \left[\frac{\sqrt{P}R^2}{D\sqrt{2vL_2\eta}} - 1\right]\frac{2dE}{D+d} \tag{12}$$

With the piston moving velocity maintained at a constant value, the constants in the equation are defined as $C = \frac{R^2}{D\sqrt{2vL_2\eta}}$ and $m = \frac{2dE}{D+d}$. Substituting these into **Equation 12** yields the corresponding solution.

$$P = \left(\frac{Cm - \sqrt{C_2M_2 - 4m}}{2}\right)^2 \tag{13}$$

Extrusion hysteresis volume is defined as the material volume continuously extruded owing to the recovery of syringe barrel deformation after the stepper motor stops, which can be calculated by **Equation 14**. Substituting **Equations 8, 9,** and **13** into the equation yields the extrusion hysteresis volume.

$$(S_1 - S)(L - tv) = V_{hyst} \tag{14}$$

3.2.3. Compressible fluid model

The above model neglects the compressibility of both the material and the piston during calculations. When the material is compressed during extrusion, its density varies linearly with the applied pressure under relatively low pressure conditions. Additionally, considering the large deformation of the rubber seal in the piston, the overall bulk compression coefficient of the material and piston is defined as α. The inclusion of this volumetric compression parameter is computationally essential for accurately capturing the delayed dynamic response inherent to piston-driven systems.[35]

$$\rho V = \rho_2 V(1 - P\alpha) \tag{15}$$

$$\rho = \rho_2(1 - P\alpha) \tag{16}$$

The mass conservation equation at equilibrium (**Equation 10**) is modified as follows:

$$S_1 v\frac{\rho}{(1 - P\alpha)} = Q\rho \tag{17}$$

Substituting **Equation 11** into **Equation 17** and again setting $n = 1$ yields:

$$P = \left[\frac{R^2}{D}\left(\frac{1}{2L_2\eta v}\right)^{1/2}P^{1/2}\sqrt{1 - P\alpha} - 1\right]\frac{2dE}{D+d} \tag{18}$$

Similarly, by defining $C = \frac{1}{D}\left(\frac{1}{2L_2\eta v}\right)^{\frac{1}{2}}R^2$ and $m = \frac{2dE}{D+d}$ and substituting these into **Equation 18**, we obtain:

$$P - Cm\sqrt{P}\sqrt{1 - P\alpha} = -m \tag{19}$$

Solving **Equation 19** for P yields:

$$P = \frac{C^2m^2 - 2m \pm Cm^{3/2}\sqrt{C^2m - 4 - 4\alpha m}}{2(1 + C^2m^2\alpha)} \tag{20}$$

The extrusion hysteresis volume in this case is given by:

$$\frac{(\pi D + \Delta x)^2}{4\pi(1 - P\alpha)}(L - t\Delta L) - \frac{(\pi D)^2}{4\pi}(L - t\Delta L) = V_{hyst} \tag{21}$$

3.3. Dynamic process model of extrusion hysteresis

For extrusion hysteresis, the most commonly adopted solution is the retraction method, which directly compensates for the hysteresis effect by setting retraction parameters matched to the volume of delayed extrusion. However, this approach has a critical drawback: the retraction action can draw air into the nozzle, causing defects and interfering with subsequent printing processes.

In this work, we adopt an alternative strategy of premature extrusion stop with travel speed adjustment. This method is based on a theoretical model that predicts the temporal evolution of the delayed extrusion flow rate $Q(t)$ after the piston stops. The travel speed of the print head is then dynamically controlled to ensure the residual material is uniformly distributed along the planned path.

The extrusion hysteresis flow rate after the piston stops is a time-dependent function, denoted as $Q(t)$. This flow rate is predicted to decay exponentially over time. The specific functional form and key parameters, such as the decay rate constant, are determined through theoretical analysis and experimental validation.

According to Poiseuille's law for Newtonian fluids, we obtain:

$$Q(t) = \frac{\pi R^4}{8L_2\eta} P(t) \tag{22}$$

During the extrusion hysteresis phase, as the material is continuously extruded, the deformation of the syringe barrel recovers, and the internal pressure difference gradually decreases.

According to the theory of material mechanics, the pressure evolution over time is described by:

$$P(t) = \frac{\Delta L - \int_0^t Q(\tau)d\tau / S_1}{L} E_{eq} \tag{23}$$

Substituting **Equation 23** into **Equation 22** yields the time-dependent function of the extrusion hysteresis flow rate after the piston stops moving.

$$Q(t) = \frac{\pi R^4}{8L_2\eta} E_{eq} \left(\frac{\Delta L}{L} - \frac{\int_0^t Q(\tau)d\tau}{S_1 L} \right) \tag{24}$$

where E_{eq} is the equivalent elastic modulus of the overall system, S_1 is the cross-sectional area of the syringe barrel, and ΔL is the variation in the length of material within the piston when extrusion stops.

During the extrusion process, elastic deformations occur in the piston rod, piston, and syringe barrel. The overall equivalent elastic modulus of the system is determined via the following measurement method: the syringe barrel, filled with a specific volume of material, is mounted and secured on a universal testing machine. The force-displacement relationship is then measured to obtain the overall equivalent elastic modulus, denoted as E_{eq}.

Let $C_3 = \frac{\pi R^4}{8L_2\eta}$, then **Equation 24** can be rewritten as:

$$Q(t) = C_3 P - C_3 \frac{E_{eq}}{LS_1} \int_0^t Q(\tau)d\tau \tag{25}$$

Taking the derivative of both sides of the equation and substituting the initial conditions $t = 0$ and $Q(0) = S_1 v$, we obtain:

$$Q(t)' = -C_3 \frac{E_{eq}}{LS_1} Q(t) \tag{26}$$

Finally, we obtain:

$$Q(t) = S_1 v \exp(-C_3 \frac{E_{eq}}{LS_1} t) \tag{27}$$

The final result shows that the extrusion hysteresis flow rate follows an exponential decay function with base e during the hysteresis phase, decreasing monotonically over time.

Integrating $Q(t) = S_1 v \exp(-C_3 \frac{E_{eq}}{LS_1} t)$ yields the equation for the variation of the extrusion hysteresis volume with time,

$$V(t) = \int_0^t S_1 v \exp(-C_3 \frac{E_{eq}}{LS_1} x)dx = -\frac{S_1^2 vL}{C_3 E_{eq}} \exp(-C_3 \frac{E_{eq}}{LS_1} \mathrm{t}) + C \tag{28}$$

Substituting the boundary condition $V(0) = 0$, we obtain:

$$V(t) = \int_0^t S_1 v \exp(-C_3 \frac{E_{eq}}{LS_1} x)dx = \frac{S_1^2 vL}{C_3 E_{eq}} (1 - \exp(-C_3 \frac{E_{eq}}{LS_1} \mathrm{t})) \tag{29}$$

To ensure uniform material deposition during the extrusion hysteresis phase, matching the quality achieved in steady-state extrusion, it is necessary to dynamically adjust the movement speed after the piston stops extruding. This adjustment is critical for achieving consistent extrusion.

During steady-state extrusion, defect-free material deposition yields a cross-sectional area of the deposited material described by **Equation 30**:

$$\frac{S_1 v}{v_m} = S_{stacking} \tag{30}$$

where v_m is the travel speed of the nozzle.

The cross-sectional area of the deposited material during the extrusion hysteresis process is:

$$\frac{Q(t)}{v(t)} = S_{stacking} \tag{31}$$

By combining **Equations 30** and **31**, the movement

speed during the extrusion hysteresis process can be obtained as:

$$v(t) = v_m \exp(-C_3 \frac{E_{eq}}{LS_1} t) \quad (32)$$

4. Results and discussion

As shown in Figure 2a, the gelation point of the 10 wt% gelatin hydrogel is approximately 29.8 °C. Analysis of material viscosity as a function of temperature at high shear rates (Figure 2b) shows that, within the range of 25–31 °C, viscosity decreases linearly with increasing temperature (R^2 >0.99). This linear relationship provides a critical basis for the subsequent selection of printing temperatures. To ensure the material remains in the sol state during extrusion, the temperature for all printing experiments was therefore set 2–3 °C above the gelation point.

As shown in Figure 2c, at a material temperature of 32 °C, viscosity variation was observed within 10 s for shear rates ranging from 20 to 100 s^{-1}. At a piston extrusion rate of 0.025 mm/s, the average shear rate inside the nozzle reaches approximately 70 s^{-1}, falling within this stable range. Thus, Newtonian fluid behavior is assumed for simplified calculations within this operating range.

4.1 Analysis of syringe temperature field simulation and fitting results

Precise temperature control is a prerequisite for maintaining the gelatin hydrogel in a predefined sol state, enabling the independent investigation of mechanical extrusion hysteresis. Based on the heat transfer model developed in Section 3, the steady-state temperature (T_3) of the material inside the syringe barrel under different combinations of ambient temperature (T_0) and heating set temperature (T_{hot}) was obtained via simulation, with the results presented in Table 2.

Table 2. Simulation results under different heating temperatures and ambient temperatures

T_{hot} (°C)	T_0 = 20	T_0 = 21	T_0 = 22
T_{hot} = 29	27.5321	27.6925	27.8542
T_{hot} = 30	28.3725	28.5319	28.6924
T_{hot} = 31	29.2155	29.3724	29.5318

At ambient temperatures of 20 °C and 21 °C with a heating set temperature of 29 °C, steady-state and transient temperature simulations are shown in Figure 3a–d. In all cases, the material temperature remains below the gelation point. Even after 20 minutes of insulation, a temperature difference of 2–3 °C persists between the material temperature and the heating set temperature. The heating process is thus slow and requires a long insulation time, highlighting the challenges of precise temperature control on non-industrial 3D printers and the necessity of prior temperature calibration.

As shown in Table 2, at a heating set temperature of 30 °C and an ambient temperature of 21 °C, the steady-state material temperature is 28.5319 °C. Compared with the steady-state temperature of 27.6925 °C obtained at a heating set temperature of 29 °C and an ambient temperature of 21 °C, the difference is 0.8394 °C. When the heating set temperature is held constant at 30 °C and the ambient temperature increases from 21 °C to 22 °C, the material temperature increases by only 0.1605 °C. These results indicate that the heating set temperature has a far greater influence on the steady-state temperature inside the syringe barrel than the ambient temperature, providing

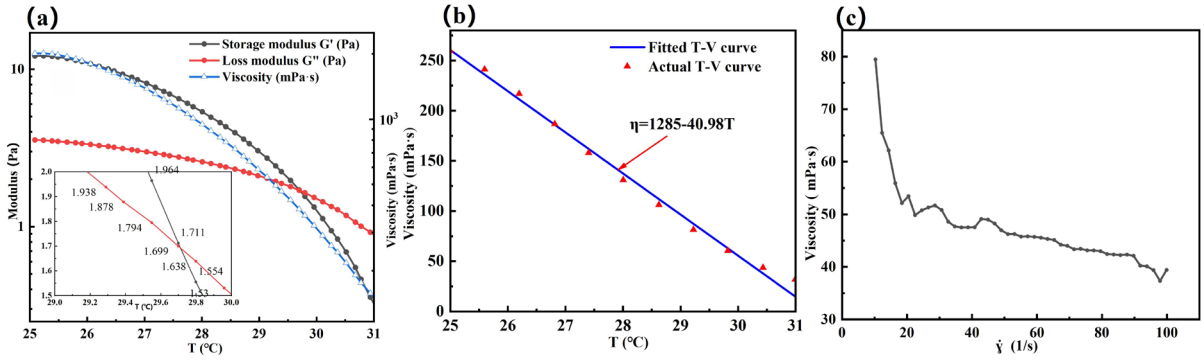

Figure 2. Rheological properties of 10 wt% gelatin. (a) Temperature sweep of the material. (b) Viscosity as a function of temperature at a shear rate of 100 s^{-1}. (c) The viscosity of pure gelatin material at 32 °C.

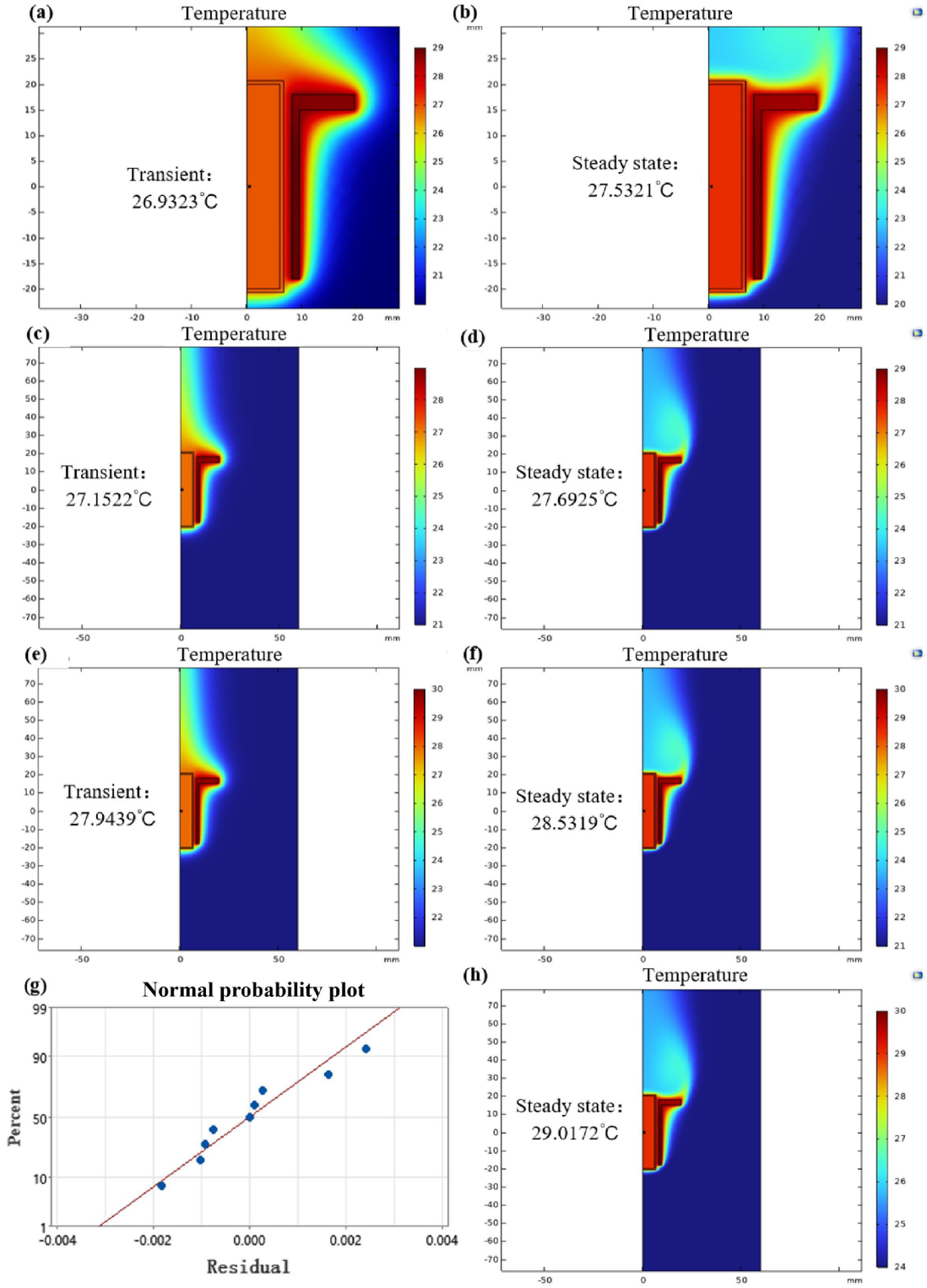

Figure 3. Temperature simulation results of the syringe barrel under different thermal conditions. (a), (b) Heating temperature 29 °C, ambient temperature 20 °C; (c), (d) Heating temperature 29 °C, ambient temperature 21 °C; (e), (f) Heating temperature 30 °C, ambient temperature 21 °C (20-min insulation); (g) Residual normal distribution of nine datasets; (h) Heating temperature 30 °C, ambient temperature 24 °C.

a key basis for the temperature control strategy adopted in this study.[36]

The data in Table 2 were imported into Minitab. A non-linear function form was predefined for fitting, with regression coefficients K_1 and K_2 treated as undetermined parameters. The final fitted temperature function is expressed as:

$$T_3 = 0.159314T_0 + 0.839574T_{hot} \quad (33)$$

Residual analysis of the linear model is presented in Figure 3g. The residuals follow an approximate normal distribution and fluctuate randomly around zero, without obvious systematic trends or heteroscedasticity. This demonstrates that the assumptions of the linear model are satisfied and the fitting performance is satisfactory.

To verify the validity of the proposed model, a validation simulation was conducted at an ambient temperature of 24 °C and a heating set temperature of 30 °C. As shown in Figure 3h, the simulated steady-state temperature is 29.0172 °C, while the model prediction yields 29.0107 °C, with an absolute error of only 0.0065 °C. The results demonstrated that the temperature prediction model possesses satisfactory accuracy and can be reliably applied to temperature regulation in subsequent experiments.

Further calculation indicates that when the heating sleeve temperature is maintained at 32 °C and the ambient temperature at 25 °C, the steady-state temperature inside the syringe barrel reaches 30.85 °C, at which the material remains in the sol state.

4.2. Experimental verification and mechanistic analysis of the static extrusion hysteresis model

Prior to establishing the extrusion hysteresis volume model, the macroscopic compression characteristics of the piston–material system were experimentally measured first. As illustrated in Figure 4, the system deformation can be divided into two distinct stages. In the initial stage (force < 30 N), displacement increases rapidly with applied force, which is primarily dominated by the large deformation of the piston seal. In the subsequent stage, the growth of displacement gradually slows down, indicating an enhanced deformation resistance of the system. Considering that the actual extrusion pressure remains relatively low, the compression coefficient α adopted in the model is calculated from the first-stage characteristic curve.

In the analysis of the effect of piston movement speed on the extrusion hysteresis volume, experiments were conducted using a nozzle with an inner diameter of 0.6 mm, an outer diameter of 0.9 mm, and a length of 18.4 mm, with the piston movement speed controlled within the range of 0.020 mm/s to 0.03 mm/s for the extrusion hysteresis tests. Figure 5e shows the images of extrusion hysteresis under different piston movement speeds and nozzle diameters. The extrusion hysteresis volume was quantified by measuring the extrusion volume of the nozzle with a diameter of 0.6 mm at various piston movement speeds. The experimental results demonstrate that the extrusion hysteresis volume increases with the increase in piston movement speed. This is because a higher extrusion speed requires a greater driving force, which induces more significant elastic deformation in the material; consequently, more elastic potential energy is stored, and a larger volume of material is released after the piston stops moving.

To minimize the influence of upward climbing of liquid material along the inner wall of the stainless steel nozzle on volume measurement, and ensure no residual liquid remains on the nozzle surface during the extrusion pause, the extrusion process starts from the edge of the printing platform. Experiments were carried out with different motion modes and extrusion speeds while using the same material formulation. At the instant of extrusion stop, the nozzle is separated from the platform, which is defined as the starting point of extrusion hysteresis. The volume of the suspended droplet is measured after the droplet stabilizes.

As shown in Figure 5a, the extrusion hysteresis volume of the material increases with the rise of piston travel speed at different temperatures, showing an approximately linear variation. Moreover, the extrusion hysteresis volume at 32 °C is slightly higher than that at 35 °C. This is because the viscosity of the material increases as the temperature decreases, which raises the extrusion pressure and consequently leads to an increase in extrusion hysteresis volume. As shown in Table 3, one-way ANOVA showed a significant main effect of extrusion speed on extrusion hysteresis volume at both temperatures (32 °C: $F(2,9) = 71.44$, $p < 0.001$; 35 °C: $F(2,9) = 56.23$, $p < 0.001$), and extrusion hysteresis volume increased significantly with increasing extrusion speed. The Tukey post-hoc test results demonstrated that at material temperatures of 35 °C and 32 °C, the differences in extrusion hysteresis volume between various extrusion speeds were statistically significant (Adjusted p <0.05).

In the analysis of the influence of nozzle diameter on the extrusion hysteresis of the material, the piston movement speed was fixed at 0.025 mm/s, and nozzles with inner diameters of 0.46 mm, 0.6 mm, and 0.75 mm were used separately.

As illustrated in Figure 5b, the extrusion hysteresis

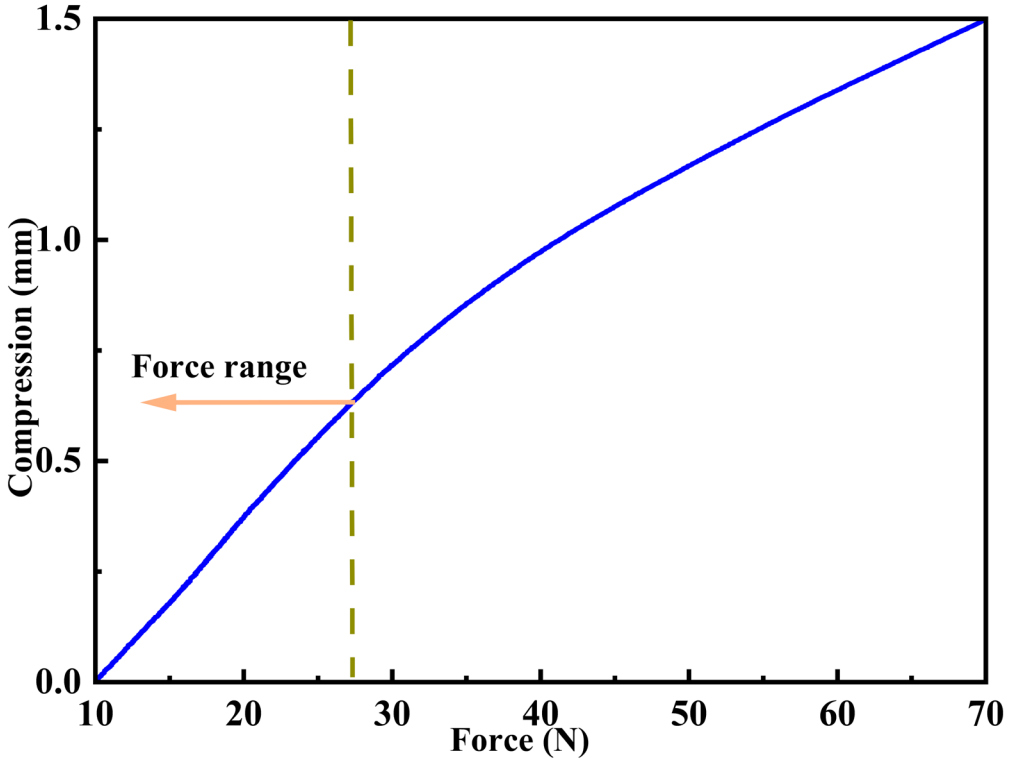

Figure 4. Force-displacement curve of the piston and material assembly

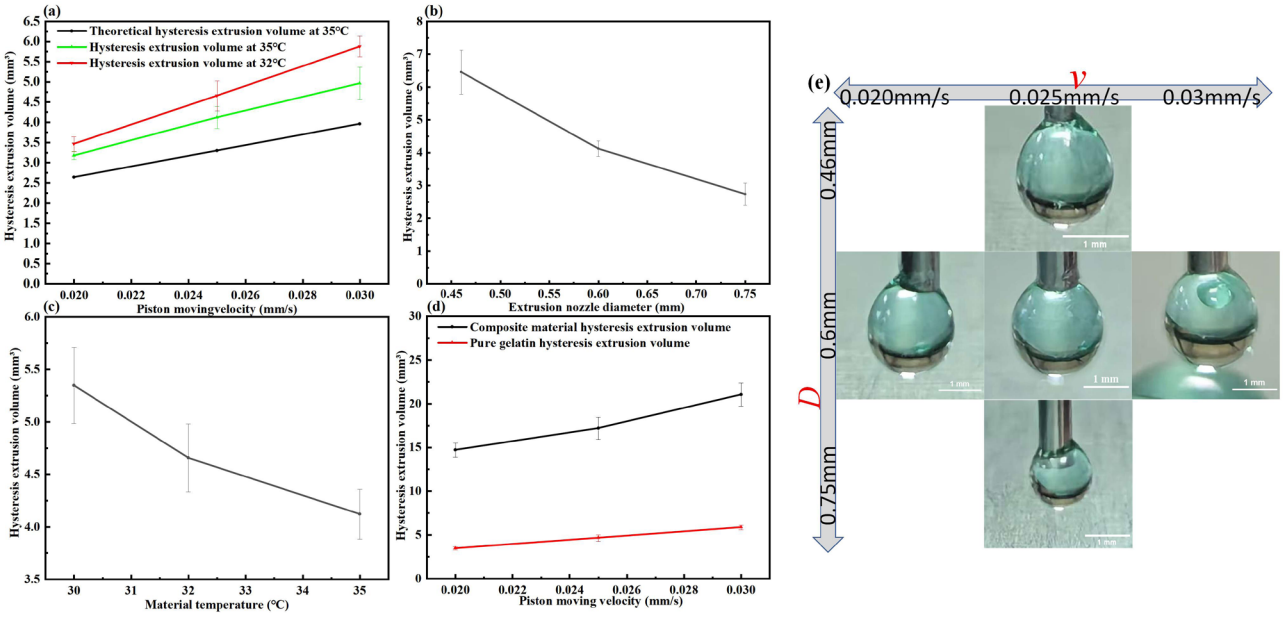

Figure 5. Variation of extrusion hysteresis volume with printing parameters. (a) Variation of extrusion hysteresis volume of pure gelatin material over time at different temperatures. (b) Variation of extrusion hysteresis volume of pure gelatin material with extrusion nozzle diameter. (c) Variation of extrusion hysteresis volume of pure gelatin material with temperature. (d) Variation of extrusion hysteresis volume of composite material and pure gelatin with temperature. (e) Corresponding extrusion hysteresis plots for different diameters and velocities (scale bars: 1 mm).

volume presents a decrease with increasing nozzle diameter. Since the pressure difference during extrusion is inversely proportional to the fourth power of the nozzle diameter, the extrusion hysteresis volume exhibits a non-linear variation with the change of nozzle diameter. As shown in Figure 5b, the changing trend does not conform to the inverse fourth-power relationship. This is because a smaller extrusion nozzle diameter corresponds to a larger specific surface area of the nozzle. The material cools down more rapidly inside the nozzle, resulting in a sharp increase in local viscosity. This hinders energy release and ultimately reduces the extrusion hysteresis volume. As shown in Table 3, one-way ANOVA showed a significant main effect of nozzle diameter on extrusion hysteresis volume ($F(2,12) = 42.07$, $p < 0.001$), and extrusion hysteresis volume decreased significantly with increasing nozzle diameter. The Tukey post-hoc test results demonstrated that the differences in extrusion hysteresis volume between the groups with extrusion head diameters of 0.46–0.60 mm and those of 0.46 mm and 0.75 mm were statistically significant (Adjusted p <0.05). In contrast, the corresponding p-value for the range of 0.6 mm–0.75 mm was 0.333 (Adjusted p > 0.05), indicating no statistically significant difference in extrusion hysteresis volume. This may be attributed to the increased gravitational effect on low-viscosity materials after an extrusion pause when using a 0.75 mm diameter extrusion head, causing downward material flow and resulting in an increased extrusion hysteresis volume. Experiments on the temperature effect on extrusion hysteresis volume were carried out at a piston travel speed of 0.025 mm/s with a 0.6 mm extrusion nozzle. As shown in Figure 5c, the extrusion hysteresis volume decreases with the increase in temperature. The reason is that the viscosity of the material increases at lower temperatures. As shown in Table 3, one-way ANOVA showed a significant main effect of temperature on extrusion hysteresis volume ($F(2,12) = 19.41$, $p < 0.001$), and extrusion hysteresis volume decreased significantly with increasing temperature. The Tukey post-hoc test results demonstrated that the volume differences in extrusion hysteresis volume of pure gelatin material across different temperatures were statistically significant (Adjusted $p < 0.05$).

Figure 5d compares the extrusion hysteresis volume of the composite material and pure gelatin under the tested conditions. Consistent with the above results, the extrusion hysteresis volume increases with the rising printing speed. Compared with pure gelatin solution at 35 °C, the composite material exhibits higher viscosity at the same temperature, which leads to a remarkable increase in extrusion hysteresis volume. As shown in Table 3, one-way ANOVA showed a significant main effect of extrusion velocity on extrusion hysteresis volume for the composite material ($F(2,12) = 44.14$, $p < 0.001$), and extrusion hysteresis volume increased significantly with increasing extrusion velocity. The Tukey post-hoc test results demonstrated that, when using composite materials, the differences in extrusion hysteresis volume between various extrusion speeds remained statistically significant (Adjusted $p < 0.05$).

In summary, the static extrusion hysteresis model was experimentally validated under key printing parameters. The extrusion hysteresis volume increases approximately linearly with piston velocity, decreases non-linearly with increasing nozzle diameter, and declines as printing temperature rises. These trends are consistent with the theoretical predictions of the compressible coupled model, confirming that extrusion hysteresis originates from the combined elastic deformation of the syringe system and the compressibility of the material. Smaller nozzles exhibit larger deviations due to accelerated heat dissipation and local gelation, while higher material viscosity leads to greater hysteresis volume. The results verify the rationality of the static model and provide a quantitative basis for parameter selection to suppress extrusion hysteresis in lowviscosity hydrogel printing.

4.3. Validation and control strategy of the dynamic extrusion hysteresis process

To investigate the temporal evolution of extrusion hysteresis volume after the piston stops, experiments were performed using a nozzle with a diameter of 0.6 mm, a piston velocity of 0.025 mm/s, and a fixed piston displacement of 1 mm. A high-speed camera was triggered immediately upon piston cessation to record the process at a frame rate of 2,000 fps. Due to the difficulty in achieving precise synchronization between the piston stop time and camera activation, **Equation 29** was rearranged accordingly.

$$\begin{aligned} Q(t) &= S_1 v \exp(-C_3 \frac{E_{eq}}{LS_1}(t+t_0)) \\ &= S_1 v \exp(-C_3 \frac{E_{eq}}{LS_1} t_0) \exp(-C_3 \frac{E_{eq}}{LS_1} t) \end{aligned} \tag{34}$$

$$\begin{aligned} V(t+t_0) &= \frac{S_1^2 vL}{C_3 E_{eq}}(1-\exp(-C_3 \frac{E_{eq}}{LS_1}(t+t_0))) + C_{res} \Rightarrow \\ &\frac{S_1^2 vL}{C_3 E_{eq}} + C_{res} - \frac{S_1^2 vL}{C_3 E_{eq}} \exp(-C_3 \frac{E_{eq}}{LS_1} t_0) \exp(C_3 \frac{E_{eq}}{LS_1} t) \end{aligned} \tag{35}$$

Table 3. One-way ANOVA results of extrusion hysteresis volume under different process conditions

Experimental condition and factor compared	*F*	(*df1*,*df2*)	*p*	η^2	Tukey pairwise comparisons	Adjusted *p*
Pure gelatin at 35 °C with different extrusion speeds	56.23	(2,9)	***$p < 0.001$	0.925	0.025–0.020	$p = 0.0012$
					0.030–0.020	$p < 0.001$
					0.030–0.025	$p = 0.0013$
Pure gelatin at 32 °C with different extrusion speeds	71.44	(2,9)	***$p < 0.001$	0.941	0.025–0.020	$p < 0.001$
					0.030–0.020	$p < 0.001$
					0.030–0.025	$p < 0.001$
Pure gelatin at 35 °C with different extrusion head diameters	42.07	(2,12)	***$p < 0.001$	0.872	0.60–0.46	$p < 0.001$
					0.75–0.46	$p < 0.001$
					0.75–0.60	$p = 0.333$
Pure gelatin under different temperatures	19.41	(2,12)	***$p < 0.001$	0.763	32–30	$p = 0.011$
					35–30	$p < 0.001$
					35–32	$p = 0.046$
Different extrusion speeds for composite materials	44.14	(2,12)	***$p < 0.001$	0.8803	0.025–0.020	$p = 0.033$
					0.030–0.020	$p < 0.001$
					0.030–0.025	$p < 0.001$

Note: *F* represents the *F*-value in analysis of variance; *df*1 and *df*2 denote the degrees of freedom between groups and within groups, respectively; *p* indicates the significance level, with ***$p < 0.001$ indicating an extremely significant difference; η^2 denotes the effect size, where $\eta^2 > 0.14$ indicates a large effect. Tukey represents the post-hoc test grouping, while adjusted *p* denotes the significance level between different groups.

In **Equation 34**, the term $-S_1 v \exp(-C_3 \frac{E_{eq}}{LS_1} t_0)$ is a constant influenced by the time interval between the piston stopping movement and the initiation of high-speed camera recording. In **Equation 35**, C_{res} denotes the volume of material suspended at the nozzle tip after the piston terminates extrusion, and the term $S_1^2 vL / (C_3 E_{eq})$ is an intrinsic constant term of the formula itself. Similarly, the term $-\frac{S_1^2 vL}{C_3 E_{eq}} \exp(-C_3 \frac{E_{eq}}{LS_1} t_0)$ is also a constant affected by the time interval between the piston stopping movement and the start of high-speed camera recording. **Equation 34** thereby provides a non-linear fitting format for the fitting model.

The images were processed using ImageJ software, where an ellipse-fitting algorithm was employed to outline the droplet profiles in Figure 6a. The major and minor axes of the ellipses were measured, and the droplet volumes were subsequently calculated via the prolate spheroid volume formula. Since the experimental setup did not allow for precise synchronization between the camera initiation time and the piston stopping moment, a more robust approach was adopted to fit the limited datasets. For the model describing the extrusion hysteresis volume as a function of time, the extrusion hysteresis volume model derived from **Equation 35** was utilized, with the exponential function using e as the base selected for fitting. The fitting results are presented in Figure 6b. Similarly, for the extrusion hysteresis flow rate model, the functional form of **Equation 34** was applied for curve fitting, as illustrated in Figure 6d.

Equations 34 and **35** demonstrate that the exponential term is consistent between the volume and flow models. Therefore, during flow-model fitting, the exponent was set to −0.434951t. The black validation points in Figure 6e indicate satisfactory results. When deriving the flow equation from the extrusion hysteresis volume, the coefficient obtained (0.760163) closely matches the predicted flow fitting model coefficient (0.746733).

To mitigate the influence of extrusion hysteresis, material extrusion was terminated in advance. The

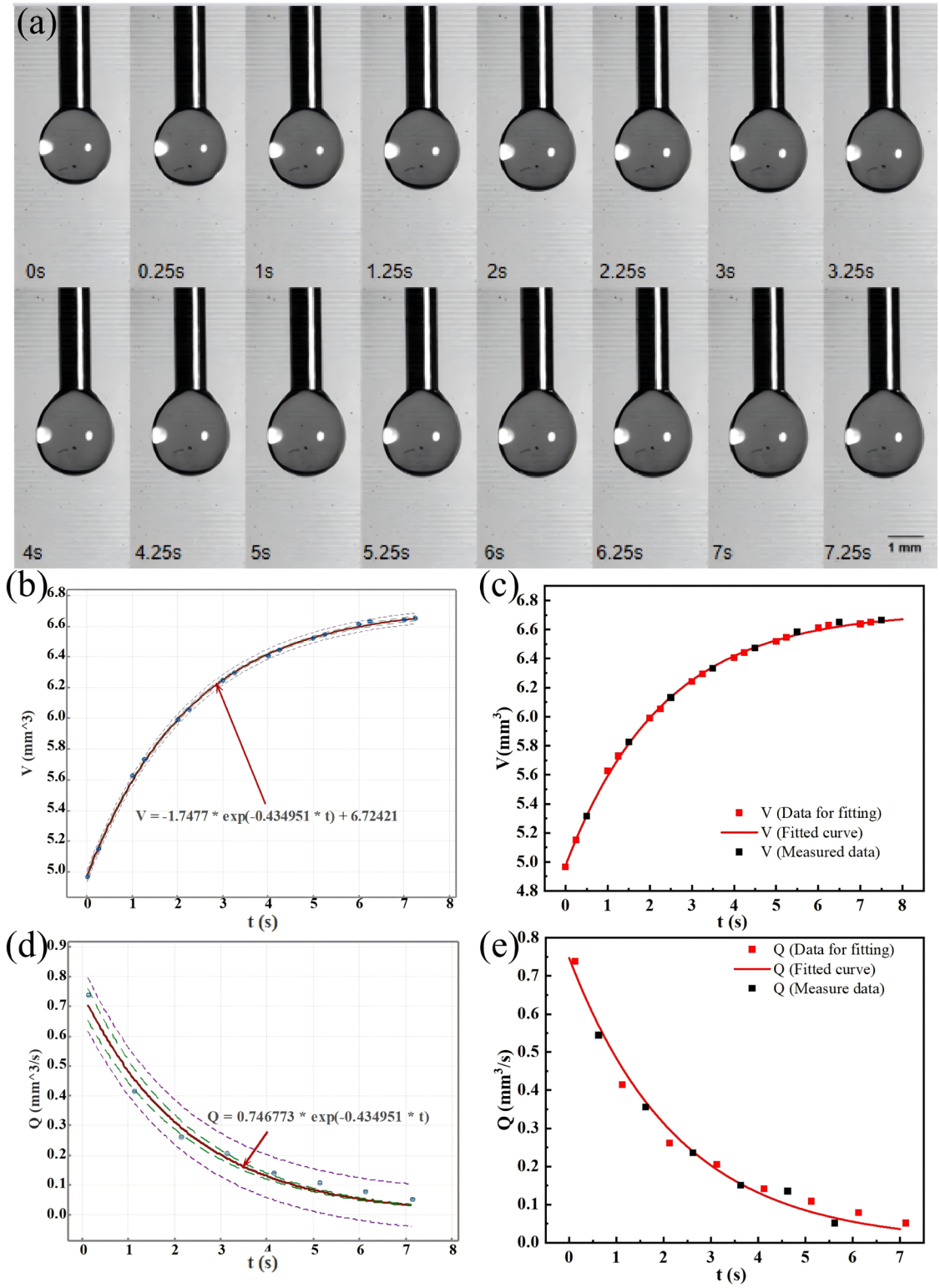

Figure 6. Dynamic change of extrusion hysteresis volume. (a) Liquid images at different time points after the start of timing; (b), (d) Fitting plots of extrusion hysteresis volume and flow rate over time; (c), (e) Validation images of the fitted extrusion hysteresis volume and flow rate.

movement speed was adjusted to ensure that the deposited cross-section maintained a consistent deposition rate equivalent to that of steady-state extrusion after the piston stopped, thus eliminating material accumulation. The effectiveness of this strategy was verified by single-layer printing of the letters "YSU," as illustrated in Figure 7.

In the experiments, the material extrusion volume was calculated based on the nozzle diameter and movement speed. When the piston extrudes pure gelatin at a velocity of 0.0125 mm/s, the nozzle moves at 5.25 mm/s. Under these parameters, the theoretical extrusion hysteresis volume is 1.5 mm^3, corresponding to an extrusion hysteresis length of approximately 5.3 mm. The extrusion stop point is therefore set 5 mm before the end of the extrusion path. After the piston stops, the movement speed of the nozzle decreases from 5.25 mm/s to 2 mm/s.

As can be seen from the comparison of the deposition areas in non-printing regions in Figure 7a–c and Table 4, the premature extrusion stop strategy eliminates material accumulation in non-printing regions. In contrast, the retraction strategy and the unoptimized printing method show little difference, with deposition areas of 34.724 mm^2 and 39.496 mm^2, respectively. For the material accumulation area within 5 mm of the letter ends, the total accumulated area at the three points under the premature extrusion stop strategy is 59.55 mm^2, which differs from the retraction strategy and the unoptimized printing method. This strategy releases the material that would otherwise accumulate in non-printing regions at the end of the printing path, thereby preventing contamination of non-printing regions and damage to the printed structure. As shown in Figure 7d–f and the comparison of deposition areas of multiple geometric patterns in non-printing regions in Table 4, this strategy remains effective in reducing material accumulation in non-printing regions during multi-pattern printing.

During printing with composite materials, the extrusion hysteresis volume varies due to changes in material viscosity, leading to differences in printing performance compared to single-layer printing with pure gelatin under identical printing parameters. As indicated by the comparison of deposition areas in non-printing regions shown in Figure 8a–c and Table 5, the premature extrusion stop strategy cannot eliminate material accumulation in non-printing regions under the same parameters, but it can significantly reduce the accumulated area. The deposition area in non-printing regions is 54 mm^2, while those of the retraction strategy and the unoptimized printing method are 146.017 mm^2 and 154.5456 mm^2, respectively.

Regarding the material accumulation area within 5 mm of the letter ends, the total accumulated area at three points under the premature extrusion stop strategy is 59.949 mm^2, while those of the retraction strategy and the unoptimized printing method are 21.73 mm^2 and

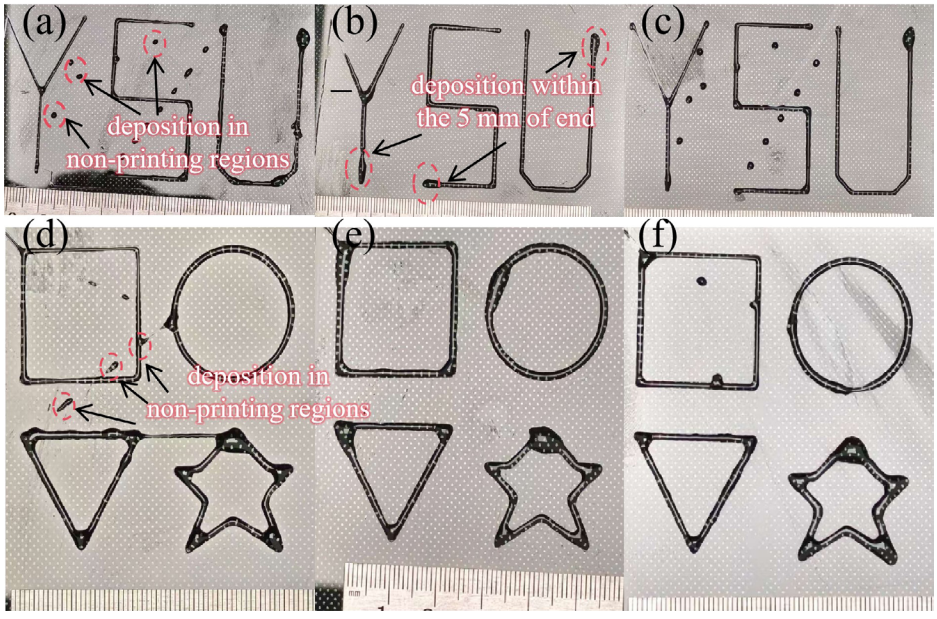

Figure 7. Single-layer printing results of pure gelatin hydrogel under different extrusion-hysteresis control strategies. (a, d) Unoptimized; (b, e) Premature extrusion stop with speed adjustment; (c, f) Conventional retraction method.

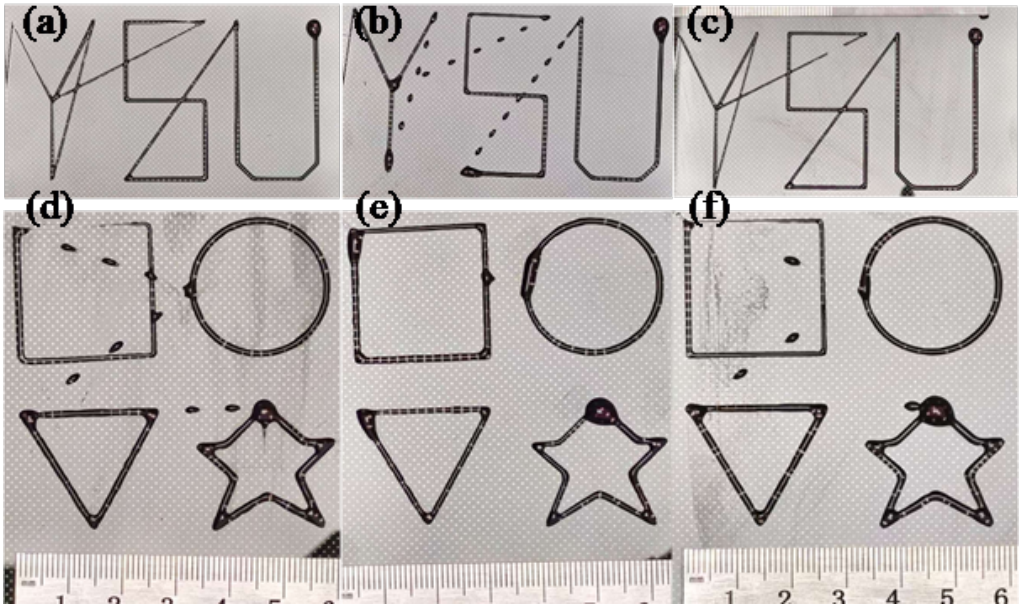

Figure 8. Single-layer pattern-printing results of the composite hydrogel under different extrusion hysteresis control strategies. (a, d) Unoptimized; (b, e) Premature extrusion stop with speed adjustment; (c, f) Conventional retraction strategy.

Table 4. Material deposition area of gelatin material under different control strategies during printing

Deposition region evaluated	Unoptimized	Premature extrusion stops with speed adjustment	Retraction
Deposition area in non-printing regions during letter printing (mm^2)	39.496 (13)	0 (0)	34.724 (11)
Deposition area within 5 mm of letter ends (mm^2)	40.767 (3)	59.55 (3)	37.846 (3)
Deposition area in non-printing regions during multi-pattern printing (mm^2)	18.551 (6)	0 (0)	7.885 (3)

Note: Values are presented as deposition area in mm^2, followed by the number of deposition points in parentheses. For example, 39.496 (13) indicates a deposition area of 39.496 mm^2 across 13 deposition points.

Table 5. Deposition area of composite materials under different control strategies during printing

Deposition region evaluated	Unoptimized	Premature extrusion stops with speed adjustment	Retraction
Deposition area in non-printing regions during letter printing (mm^2)	154.5456 (3 lines)	54 (18 points)	146.017 (4 lines)
Deposition area within 5 mm of letter ends (mm^2)	23.78 (1 point)	59.949 (3 points)	21.73 (1 point)
Deposition area in non-printing regions during multi-pattern printing (mm^2)	28.946 (8 points)	2.746 (1 point)	15.786 (4 points)

Note: Values are presented as deposition area in mm^2, followed by the number and type of deposition features in parentheses. For example, 54 (18 points) indicates a deposition area of 54 mm^2 across 18 deposition points.

23.78 mm^2, respectively. This discrepancy arises from the increased viscosity, which prolongs the material release time during extrusion hysteresis. Due to the short residence time after completing the letter printing, less hysteresis volume is released, resulting in almost no excess accumulation at the ends of letters Y and S. Therefore, only the area at the end of letter U was selected to calculate the accumulation area within 5 mm for the retraction strategy and the unoptimized printing method. As shown in Figure 8d–f and the comparison of deposition areas of multiple geometric patterns in non-printing regions in Table 5, this strategy remains effective in reducing material accumulation in non-printing regions during multi-pattern printing.

Under the same printing parameters, the extrusion hysteresis volume of the composite material reaches 7 mm^3, with a corresponding extrusion hysteresis length of approximately 20 mm. If the conventional retraction strategy is adopted, excessive material will be drawn back into the syringe barrel, which can easily introduce air and contaminate the material inside. Repeated retraction may lead to air accumulation in the barrel, interfering with subsequent printing. Thus, the required retraction volume can only be reduced by lowering the printing speed.

For the premature extrusion stop strategy proposed in this work, an extrusion hysteresis length of 20 mm is also challenging. This length can be reduced by decreasing the printing speed or increasing the nozzle diameter. However, in single-layer or continuous printing, this strategy can utilize the continuous printing path to provide sufficient time and distance for the release of extrusion hysteresis material.

A comparison between Figure 9a–c and Figure 9d–f, as well as the data in Table 6, reveals that when the premature extrusion stop strategy is adopted to control material deposition in non-printing regions during experiments with the composite material, the material deposition area in non-printing regions shows a clear decreasing trend as the printing speed is reduced. For the 0.6 mm nozzle, the deposition area decreases from 54 mm^2 to 28.037 mm^2, and the material accumulation within 5 mm of the letter ends decreases from 59.949 mm^2 to 40.275 mm^2. The same trend is observed with the 0.75 mm nozzle. This phenomenon occurs because the extrusion hysteresis volume decreases with the reduction in printing speed.

Further comparison of Figure 9a and 9d, Figure 9b and 9e, and Figure 9c and 9f indicates that as the nozzle diameter increases, both the material deposition in non-printing regions and the deposition area within 5 mm of the letter ends decrease. This is because a larger nozzle diameter lowers the internal pressure and reduces the hysteresis volume, thereby decreasing material deposition in non-printing areas.

Figure 9g shows a continuous annular pattern printed using a deceleration strategy, in which the printing speed was reduced to 5.25 mm/s to 2 mm/s over the final 20 mm of the path to release material accumulated due to extrusion hysteresis. The line width of the hysteresis section exhibits a gradual transition from thick to thin, suggesting that the adopted speed is not optimal. Theoretically, stepped speed control can produce more uniform line width and reduce material accumulation at the end point, and such speed control is closely related to the rheological properties of the material.

From these experiments, it can be found that the premature extrusion stop strategy can effectively suppress material accumulation in non-printing regions, with a significantly better performance than the retraction

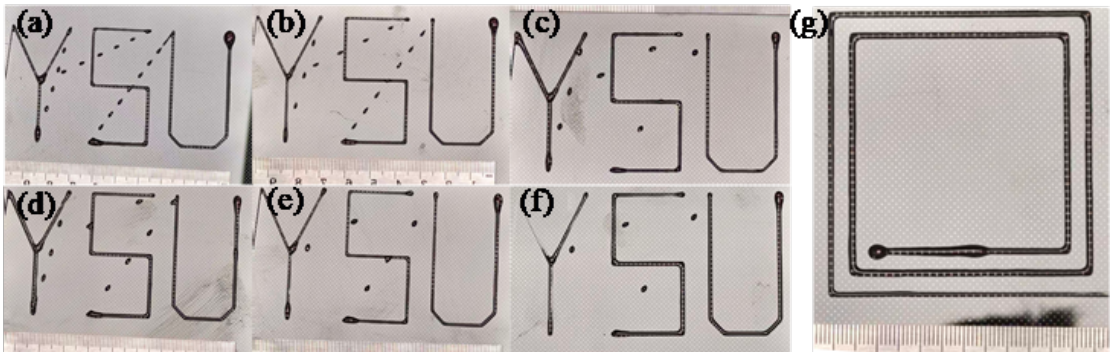

Figure 9. Printing performance of single-layer patterns using composite materials under the premature extrusion stop control strategy at different speeds and nozzle diameters. (a–c) Nozzle diameter: 0.6 mm, printing speeds: 5.25 mm/s, 3.5 mm/s, and 2.625 mm/s, respectively; (d–f) Nozzle diameter: 0.75 mm, printing speeds: 5.25 mm/s, 3.5 mm/s, and 2.625 mm/s, respectively ; (g) Continuous annular pattern printed at a normal speed of 5.25 mm/s, and with a speed of 2 mm/s for the final 20 mm section.

Table 6. Material deposition area of composite material at different printing speeds and nozzle diameters

Printing speed (mm/s)	5.25 mm/s	3.5 mm/s	2.625 mm/s
Deposition area in non-printing regions (0.6 mm nozzle; mm^2)	54 (18)	38.037 (13)	28.037 (8)
Deposition area within 5 mm of letter ends (0.6 mm nozzle; mm^2)	59.949 (3)	48.79 (3)	40.275 (3)
Deposition area in non-printing regions (0.75 mm nozzle; mm^2)	28.742 (9)	20.881 (5)	15.371 (4)
Deposition area within 5 mm of letter ends (0.75 mm nozzle; mm^2)	49.697 (3)	43.408 (3)	36.222 (3)

Note: Values are presented as deposition area in mm^2, followed by the number and type of deposition features in parentheses. For example, 54 (18 points) indicates a deposition area of 54 mm^2 across 18 deposition points.

strategy. This is because the printing path of the unextruded portion is utilized to reduce the impact of material on non-printing regions, resulting in a small amount of material accumulation within 5 mm at the end of the printing path. Furthermore, the accumulation area of material in non-printing regions and at the letter ends can be reduced by decreasing the printing speed and increasing the nozzle diameter.

This section summarizes our three core findings: a coupled extrusion hysteresis model, the exponential decay law of hysteresis flow rate, and a model-based dynamic control strategy. This method is suitable for printing materials with a viscosity similar to that in the experiment. The most critical objective is to eliminate the adverse effects of unintended material extrusion on print quality, which occurs either at the end of the printing process or during non-extruding movements of the print head between different positions.

5. Conclusion and future work

This study addresses the extrusion hysteresis phenomenon of hydrogels in piston-extrusion 3D printing. By integrating the rheological properties of the material, the structural deformation of the system, and the temperature distribution law, a prediction model for the extrusion hysteresis volume was established, and its mechanism was revealed. The results demonstrated that, within the tested ranges of piston movement speed (0.020–0.03 mm/s) and nozzle diameter (0.46–0.75 mm), the predicted response pattern was consistent with the experimental measurements, effectively characterizing the relationship between key printing parameters and the extrusion hysteresis volume.

Simulation results show that the material temperature inside the syringe barrel exhibits a linear relationship with both the set heating temperature and the ambient temperature. The heating temperature has a dominant effect on the material temperature, while the influence of ambient temperature is relatively minor. Due to the high specific heat capacity of water, the transient simulation indicates that the material still fails to reach thermal equilibrium even after 20 minutes of heating. Therefore, precise control of the heating temperature is critical for maintaining the material state within the barrel. Furthermore, the abrupt viscosity change of the material near its gelation point directly affects both the continuity of the extrusion process and the extrusion hysteresis volume.

The study found that the extrusion hysteresis volume increases with increasing piston speed and decreases with increasing nozzle diameter. This is because higher speeds and smaller nozzle diameters lead to greater deformation of the piston and barrel, thereby releasing more elastic potential energy. Additionally, within the range of conditions investigated, increases in viscosity caused by material changes and temperature variations all result in an increase in the extrusion hysteresis volume.

In summary, the control strategy of "premature extrusion stop with speed adjustment" can effectively reduce material deposition during non-printing nozzle movements. Both this strategy and the retraction strategy perform well when printing low-viscosity materials. However, as viscosity increases, the same retraction parameters are no longer effective, and further increasing retraction volume risks air ingestion and material contamination. During continuous printing processes, sufficient time is available for the release of the extrusion hysteresis volume.

This model holds practical guiding significance for the optimization of self-assembled bioprinters. By adjusting the nozzle dimensions and optimizing the design of the heating sleeve, the extrusion hysteresis effect can be mitigated, providing a reference for the printing of low-viscosity hydrogels. However, this model has limitations: it is only applicable to materials with similar viscosity to those used in this study, and the material must be

maintained above its gelation point in a fully sol state. When the material transitions to a gel state, its rheological behavior becomes highly complex, and the present model is no longer valid.

For low-viscosity materials, spreading is unavoidable; therefore, printing accuracy remains an issue that requires in-depth consideration. Future work must address the problem of material spreading during printing to better realize the application value of this work in the field of bioprinting. For instance, some studies have employed fast-setting materials or low-temperature platforms to enable low-viscosity materials to rapidly acquire shape-retaining capabilities on the platform. Additionally, ongoing research is exploring the integration of a mesh platform beneath the nozzle to suppress material spreading and provide structural support. This printing strategy offers useful guidance for future low-viscosity hydrogel printing.

Acknowledgments

The authors gratefully acknowledge the School of Mechanical Engineering, Yanshan University, for providing a critical experimental platform and technical support throughout this work. We also thank the State Key Laboratory of Crane Technology at Yanshan University for equipment assistance.

Funding

This work is supported by the National Natural Science Foundation of China (52305513, 52575542, 52305425), Science Research Project of Hebei Education Department (BJK2024053), and Collaboration projects between universities in Hebei and Shijiazhuang City (241791107A).

Conflict of interest

The authors declare that they have no known competing financial interests or personal relationships that could have appeared to influence the work reported in this paper.

Author contributions

Conceptualization: Haoran Ren, Zhen Wang
Data curation: Haoran Ren
Formal analysis: Haoran Ren
Funding acquisition: Zhen Wang
Investigation: Haoran Ren, Longhua Xu, Shuiquan Huang, Meina Qu, Zhengkai Xu, Dijia Zhang, Baosu Guo, Tianye Jin, Xiaodan Wang, Bowen Li
Methodology: Haoran Ren, Zhen Wang, Chuanzhen Huang
Project administration: Zhen Wang
Resources: Zhen Wang, Chuanzhen Huang
Software: Haoran Ren
Supervision: Zhen Wang, Chuanzhen Huang
Validation: Haoran Ren, Zhen Wang
Visualization: Haoran Ren
Writing–original draft: Haoran Ren
Writing–review & editing: Zhen Wang, Chuanzhen Huang

Ethics approval and consent to participate

Not applicable.

Consent for publication

Not applicable.

Availability of data

All relevant data are available within the manuscript.

References

1. Richards D, Jia J, Yost M, Markwald R, Mei Y. 3D Bioprinting for Vascularized Tissue Fabrication. *Ann Biomed Eng*. 2017;45(1):132-147.

   doi: 10.1007/s10439-016-1653-z

2. He P, Zhao JN, Zhang JM, *et al*. Bioprinting of skin constructs for wound healing. *Burns Trauma*. 2018;6:10.

   doi: 10.1186/s41038-017-0104-x

3. Daly AC, Critchley SE, Rencsok EM, Kelly DJ. A comparison of different bioinks for 3D bioprinting of fibrocartilage and hyaline cartilage. *Biofabrication*. 2016;8(4):045002.

   doi: 10.1088/1758-5090/8/4/045002

4. Zhang JH, Wehrle E, Rubert M, Müller R. 3D Bioprinting of Human Tissues: Biofabrication, Bioinks, and Bioreactors. *Int J Mol Sci*. 2021;22(8):3971.

   doi: 10.3390/ijms22083971

5. Teixeira MC, Singh KK, de Melo BAG, Severino P, Cardoso JC, Souto EB. 3D bioprinting: An innovative technique for biofabrication applied to regenerative medicine and tissue engineering. In: *Nanotechnology and Regenerative Medicine*. Amsterdam, Netherlands: Elsevier; 2023:195-232.

   doi: 10.1016/b978-0-323-90471-1.00012-8

6. Matai I, Kaur G, Seyedsalehi A, McClinton A, Laurencin CT. Progress in 3D bioprinting technology for tissue/organ regenerative engineering. *Biomaterials*. 2020;226:119536.

   doi: 10.1016/j.biomaterials.2019.119536

7. Ning LQ, Chen XB. A brief review of extrusion-based tissue scaffold bio-printing. *Biotechnol J*. 2017;12(8):18.

   doi: 10.1002/biot.201600671

8. Thareja P, Swarupa S, Ahmad S, Jinugu ME. Hydrogel-based inks for extrusion 3D printing: A rheological viewpoint. *Curr Opin Colloid Interface Sci*. 2025;77:101918.

   doi: 10.1016/j.cocis.2025.101918

9. 3D extrusion bioprinting. *Nat Rev Methods Primers*. 2021;1(1).

   doi: 10.1038/s43586-021-00078-3

10. Zhou LL, Su SH. Design and Validation of a Piston-Driven Syringe-Extrusion Bioprinter Using an FDM Frame. *Biomimetics*. 2025;10(12):811.

    doi: 10.3390/biomimetics10120811

11. Sun W, Wan Y. *Biomaterials 3D Printing: Technology and Application*. Beijing, China: Science Press; 2022:49-71.

12. da Fonseca JHL, Corzo IJM, Azoubel RA, *et al*. Real-time force and rheological measurement for hydrogels 3D bioprinting using a piston-driven extrusion system. *Bioprinting*. 2025;52:e00446.

    doi: 10.1016/j.bprint.2025.e00446

13. Ramesh S, Harrysson OLA, Rao PK, *et al*. Extrusion bioprinting: Recent progress, challenges, and future opportunities. *Bioprinting*. 2021;21.

    doi: 10.1016/j.bprint.2020.e00116

14. Fisch P, Holub M, Zenobi-Wong M. Improved accuracy and precision of bioprinting through progressive cavity pump-controlled extrusion. *Biofabrication*. 2021;13(1):18.

    doi: 10.1088/1758-5090/abc39b

15. Gómez-Blanco JC, Pagador JB, Galván-Chacón VP, *et al*. Computational simulation-based comparative analysis of standard 3D printing and conical nozzles for pneumatic and piston-driven bioprinting. *Int J Bioprint*. 2023;9(4):730.

    doi: 10.18063/ijb.730

16. Woods P, Smith C, Clark S, Habib A. Integrating Pneumatic and Thermal Control in 3D Bioprinting for Improved Bio-Ink Handling. *Designs*. 2024;8(4):83.

    doi: 10.3390/designs8040083

17. Bonatti AF, Vozzi G, Chua CK, De Maria C. A Deep Learning Quality Control Loop of the Extrusion-based Bioprinting Process. *Int J Bioprint*. 2022;8(4):620.

    doi: 10.18063/ijb.v8i4.620

18. Moroni L, Boland T, Burdick JA, *et al*. Biofabrication: A Guide to Technology and Terminology. *Trends Biotechnol*. 2018;36(4):384-402.

    doi: 10.1016/j.tibtech.2017.10.015

19. Ribeiro A, Blokzijl MM, Levato R, *et al*. Assessing bioink shape fidelity to aid material development in 3D bioprinting. *Biofabrication*. 2018;10(1):9.

    doi: 10.1088/1758-5090/aa90e2

20. Cooke ME, Rosenzweig DH. The rheology of direct and suspended extrusion bioprinting. *APL Bioeng*. 2021;5(1):011502.

    doi: 10.1063/5.0031475

21. Unagolla JM, Jayasuriya AC. Hydrogel-based 3D bioprinting: A comprehensive review on cell-laden hydrogels, bioink formulations, and future perspectives. *Appl Mater Today*. 2020;18:100479.

    doi: 10.1016/j.apmt.2019.100479

22. Herrada-Manchón H, Fernández MA, Aguilar E. Essential Guide to Hydrogel Rheology in Extrusion 3D Printing: How to Measure It and Why It Matters? *Gels*. 2023;9(7):21.

    doi: 10.3390/gels9070517

23. Gao T, Gillispie GJ, Copus JS, *et al*. Optimization of gelatin-alginate composite bioink printability using rheological parameters: a systematic approach. *Biofabrication*. 2018;10(3):9.

    doi: 10.1088/1758-5090/aacdc7

24. Yin J, Yan ML, Wang YC, Fu JZ, Suo HR. 3D Bioprinting of Low-Concentration Cell-Laden Gelatin Methacrylate (GelMA) Bioinks with a Two-Step Cross-linking Strategy. *ACS Appl Mater Interfaces*. 2018;10(8):6849-6857.

    doi: 10.1021/acsami.7b16059

25. Zhou Y, Liao SL, Chu YJ, *et al*. An injectable bioink with rapid prototyping in the air and in-situ mild polymerization for 3D bioprinting. *Biofabrication*. 2021;13(4):045026.

    doi: 10.1088/1758-5090/ac23e4

26. Palacín-García R, Goñi L, Gómez-del Río T. Exploring the Rheological Properties of 3D Bioprinted Alginate-Based Hydrogels for Tissue Engineering. *Biomimetics*. 2025;10(8):491.

    doi: 10.3390/biomimetics10080491

27. Schwab A, Levato R, D'Este M, Piluso S, Eglin D, Malda J. Printability and Shape Fidelity of Bioinks in 3D Bioprinting. *Chem Rev*. 2020;120(19):10850-10877.

    doi: 10.1021/acs.chemrev.0c00084

28. Chen X, Anvari-Yazdi AF, Duan X, *et al*. Biomaterials / bioinks and extrusion bioprinting. *Bioact Mater*. 2023;28:511-536.

    doi: 10.1016/j.bioactmat.2023.06.006

29. Ouyang LL, Yao R, Zhao Y, Sun W. Effect of bioink properties on printability and cell viability for 3D bioplotting of embryonic stem cells. *Biofabrication*. 2016;8(3):12.

    doi: 10.1088/1758-5090/8/3/035020

30. Zhang CL, Elvitigala K, Mubarok W, Okano Y, Sakai S. Machine learning-based prediction and optimisation framework for as-extruded cell viability in extrusion-based 3D bioprinting. *Virtual Phys Prototyp*. 2024;19(1):e2400330.

    doi: 10.1080/17452759.2024.2400330

31. Gao Q, Yu KC, Chen FZ, Lu LH, Zhang P. Investigation on the Temperature Distribution Uniformity of an Extrusion-Based 3D Print Head and Its Temperature Control

Strategy. *Pharmaceutics*. 2022;14(10):15.

doi: 10.3390/pharmaceutics14102108

32. Incropera FP, DeWitt DP, Bergman TL, Lavine AS, Ge X, Ye H. *Fundamentals of Heat and Mass Transfer*. 6th ed. Beijing, China: Chemical Industry Press; 2025:2-9.

33. Hibbeler RC, Wang Y. *Mechanics of Materials*. Beijing, China: Publishing House of Electronics Industry; 2006:89-94.

34. Zhang M, Jing S, Li G. *Advanced Engineering Fluid Mechanics*. Xi'an, China: Xi'an Jiaotong University Press; 2006:73-78.

35. Li BW, Huang CZ, Wang Z, *et al*. Modeling of Extrusion 3D Bioprinting Precision Considering the Non-Newtonian Rheological Dynamics of Gelatin-Chitosan Hydrogels. *ACS Appl Polym Mater*. 2025;7(3):1257-1270.

doi: 10.1021/acsapm.4c02866

36. He Y, Yang FF, Zhao HM, Gao Q, Xia B, Fu JZ. Research on the printability of hydrogels in 3D bioprinting. *Sci Rep*. 2016;6:13.

doi: 10.1038/srep29977